Wavefront reconstruction of a non-diffracting structured laser beam

MARTIN DUSEK,[1,2,*] ![ORCID] JEAN-CHRISTOPHE GAYDE,[1] AND MIROSLAV SULC[2,3]

[1]*The European Organization for Nuclear Research (CERN), Geneva, Switzerland*
[2]*Technical University of Liberec (TUL), Liberec, Czech Republic*
[3]*Institute of Plasma Physics of the Czech Academy of Sciences (IPP CAS), Prague, Czech Republic*
*martin.dusek@cern.ch

Abstract: The Structured Laser Beam (SLB) is a pseudo-non-diffracting laser beam that shares many characteristics with a Bessel beam. However, it can theoretically propagate over an unlimited distance while maintaining an extremely low inner core divergence of only 0.01 mrad. This makes it a promising candidate for precise long-distance alignment applications such as the alignment of particle accelerator components at CERN. In this work, a novel method to assess the symmetrical wavefront aberrations induced by an SLB generator is presented. Our approach is based on the analysis of a single-intensity distribution of an SLB. The coefficients of the Zernike polynomials are estimated using artificial intelligence before least-squares fitting is used to refine the result. This approach ensures that the fitting avoids local minima. This method provides a novel way to analyze the optical aberrations induced by the SLB generator.

1. Introduction

Accurately aligning accelerator components over long distances poses a significant challenge, requiring precision of the transversal position in the range of tens of micrometers over distances of hundreds of meters. At CERN, straight-line reference systems have been developed to meet these stringent accuracy requirements [1]. These systems, such as the Wire Positioning System and Hydrostatic Leveling System, use physical references, in these cases stretched wires and water levels, respectively. While highly precise, they suffer from implementation difficulties and component costs and are difficult to scale to even larger accelerators. An optical-based system could serve as a viable alternative for future colliders like the Compact Linear Collider (CLIC) [2] or the Future Circular Collider (FCC) [3], which are currently under study at CERN. These projects require tight alignment tolerances in the transversal direction, with an accuracy of up to 10 μm (1σ) over a 200 m span [4]. Several optical-based systems for aligning structures over long distances have been proposed in various works [4–9], however, the drawback of these systems is their relatively high divergence, which makes it challenging to achieve accurate straight-line reference measurements over long distances.

A promising candidate to overcome this drawback is the Structured Laser Beam (SLB) [10]. The SLB is a pseudo-non-diffracting beam with a transversal intensity profile similar to a Bessel Beam (BB) of zeroth order [11,12]. It shares certain properties with the BB, such as a low divergence of the central core compared to a Gaussian Beam (GB) and the ability for regeneration behind obstacles [13]. Various reports have explored the use of pseudo-non-diffracting beams for alignment purposes. Parks [14–17] used BB for aligning optical elements, while Gale [18] employed projected BB for aligning larger structures over 19 m. However, contrary to a BB, the SLB maintains a well-defined central core that can fit on a reasonably sized sensor chip even after propagating for several hundred meters. Propagation tests up to 900 m have been conducted at

CERN, yielding a divergence of under 0.01 mrad. This enables direct reading of the SLB image using a reasonably sized camera chip even after propagation over hundreds of meters.

The generation principle for an SLB relies on utilizing the symmetrical optical aberrations, namely defocus and spherical aberrations, and is described in detail in subsequent sections. It is crucial to know the values of the defocus and spherical aberrations to determine SLB properties. Some studies have addressed the issue of aberrated BBs produced by oblique illumination of an axicon or a diffracting element [19–21]. Dudutis [22] demonstrated the use of these aberrated beams for glass dicing. Khonina presented a method for analyzing astigmatic BBs to detect birefringence of gradient-index lenses and crystals [23,24] and presented a way to analyze the intensity distribution of optical aberrations for a combination of an axicon and bi-convex lens [25]. Miao [26] proposed a technique for phase front retrieval and correction of a BB. However, none of these works presented a fast and reliable method for assessing wavefront aberrations in beams generated solely by symmetrical optical aberrations, such as an SLB.

To evaluate the wavefront shape, traditional wavefront sensing methods can be employed. However, this approach can be problematic since the wavefront should be measured directly behind the projection lens. In the context of long-distance alignment applications, the SLB propagates within a vacuum pipe, making it challenging to directly measure the wavefront immediately behind the generator. The considerable diameter of the generator projection lens can also introduce complexities in measurements using conventional wavefront sensing methods. This paper presents a simple method for estimating the wavefront of an SLB utilizing a combination of a convolutional neural network (CNN) and least-square fitting. While there have been reports of using artificial intelligence (AI) for detecting wavefront aberrations [27–29], to the best of our knowledge, AI has not been employed for wavefront analysis of non-diffracting beams. This method enables the determination of the SLB dominant symmetrical wavefront aberrations using a single SLB intensity distribution, with application to high-precision, long-distance alignment, where it can provide information about the beam properties.

2. Methodology

The SLB can be generated using various generators that create a uniquely shaped wavefront by combining rotationally symmetrical aberrations: spherical aberration, secondary spherical aberration and defocus. Such an optical system functions as a Keplerian beam expander, maintaining the nearly parallel nature of both input and output beams while introducing a phase delay. This phase delay results in a distinctive wavefront shape. It is important to note that this wavefront is formed directly behind the projection lens, as depicted in Fig. 1. As one moves farther from the generator along the direction of SLB propagation, various segments of the wavefront undergo constructive and destructive interference, resulting in an intensity distribution resembling that of a Bessel Beam. However, in the case of SLB, there is a radial intensity modulation of the beam's rings. The shape of the wavefront directly influences beam properties, including the core size, the number of rings, and their intensity modulation. A critical parameter in this context is the so-called zero-phase gradient ring, depicted in Fig. 2, which can be utilized to determine the central core size [30].

An SLB can be generated using a variety of generators. In this work, a 5 mm ball lens made of N-BK7 glass is used in combination with a plano-convex projection lens. The projection lens is made of N-BK7 glass with a diameter of 9 mm and a radius of curvature of 10.3 mm. By changing the distance between the lenses, denoted as L_{PL} in the interval L_{PLMIN} to L_{PLMAX}, the diameter of the zero-phase gradient ring is changed, affecting the core size as illustrated in Fig. 2.

The values of L_{PLMIN} and L_{PLMAX} were equal to 18.8 and 19.25 mm respectively. This interval of values ensures that the SLB pattern can fit into a 10x10 mm region of interest on a Basler camera acA4112-30uc featuring a CMOS chip measuring 14.13x10.35 mm placed 1.5 m away from the generator. The limitations of our experimental setup defined this constraint. The shorter
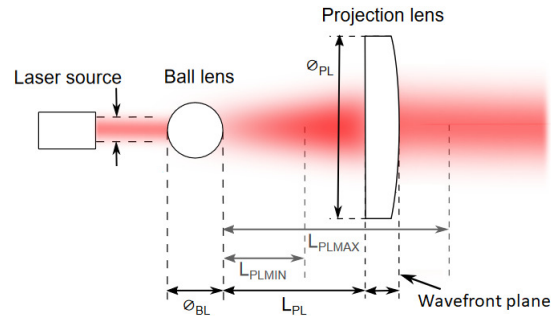
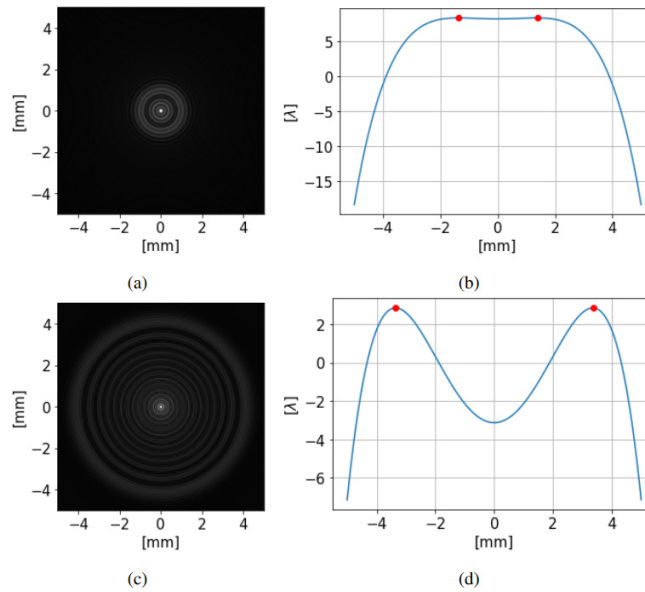**Fig. 1.** Schematic of an SLB generator.

Fig. 2. Simulated intensity distributions and corresponding line profiles using Eq. (3) traced to z = 1.5 m. (a) c_j values corresponding to L_{PLMAX} producing a core size of 0.26 mm (b) the corresponding wavefront profile. The zero-phase gradient ring is highlighted by red dots having a diameter of 2.81 mm. (c) c_j values corresponding to L_{PLMIN} producing a core size of 0.16 mm (d) the corresponding wavefront profile. The zero-phase gradient ring is highlighted by red dots having a diameter of 6.6 mm.

L_{PL} reduces the amount of defocus aberration in the wavefront. This affects the size of the zero-phase gradient ring diameter, which becomes larger. The SLB with a relatively small core size is created as a result at a certain distance. Other parameters, such as the number of rings and divergence, are also affected by the change of the L_{PL} distance. This generation principle allows for fast and easy tuning of the SLB core size and other parameters. More details about the generation principle can be found in our previous works [10,30,31] and in the paper of Herman [32].

A method that analyses a single transversal intensity distribution to estimate the shape of the wavefront directly behind the projection lens was proposed. The phase of the complex field behind the projection lens, hence the wavefront shape, can be described using normalized Zernike polynomials [33]. Zernike polynomials are described by Z_j and their respective coefficients c_j, The Noll indexing was used [34].

To validate the method, results were compared with measured data obtained from a Shack-Hartmann sensor (SHS). The SHS was placed as close as physically possible in front of the projection lens to measure the wavefront in the plane directly behind the projection lens. The SHS consisted of a microlens array MLA300-14AR from Thorlabs combined with a Basler camera a2A5328-15umPRO. The wavefront shape and phase were calculated using in-house software [35].

Equation (1) describes the complex field of a non-aberrated SLB, which is approximated using only defocus and spherical aberrations with index j equal to 4, 11, and 22, respectively.

$$s(x_0, y_0, 0) = S_0 exp[i2\pi(c_4 Z_4 + c_{11} Z_{11} + c_{22} Z_{22})] \tag{1}$$

Equation (2) describes a situation where other aberrations that do not contribute to the creation of a beam are present, represented as the sum of the j-number of Zernike polynomials in the complex field. These aberrations can have unwanted influence on the intensity distribution symmetry.

$$g(x_0, y_0, 0) = G_0 exp(i2\pi \sum_j c_j Z_j); j \notin \{4, 11, 22\} \tag{2}$$

If the complex field is known, a diffraction integral can be employed to propagate the field and reconstruct the transversal intensity distribution $U(x, y, z)$ at an arbitrary distance z as described by Eq. (3). In this equation, k represents the angular wavenumber and λ the wavelength of light.

$$U(x, y, z) = \frac{1}{i\lambda z} exp(ikz) exp[\frac{ik(x^2 + y^2)}{2z}] FT\{s(x_0, y_0, 0)g(x_0, y_0, 0)exp[(x_0^2 + y_0^2)\frac{ik}{2z}]\} \tag{3}$$

The method presented here deals with the inverse task. The intensity distribution $I(x, y)$ of the SLB is measured using a CMOS chip at a given distance from the projection lens. This measurement serves as input for a non-linear-least-squares minimization of the c_4, c_{11} and c_{22} values to match the measured intensity distribution $I(x, y)$ at a given distance z according to the Eq. (4) [26]. We assume $g(x_0, y_0, 0) = 0$ for the fitting process. This estimation is allowed by the fact that, in reality, the values of aberrations expressed by $g(x_0, y_0, 0)$ are small. This will become evident in the following chapters. $S_0 = 1$ was also assumed.

$$S = \min_{c_4, c_{11}, c_{22}} \sum_x \sum_y [U(x, y, z) - I(x, y)]^2 \tag{4}$$

When the minimization process begins with coefficient values equal to zero or random values, the fitting process becomes trapped in a local minimum, failing to determine the values of the polynomials even for least-squares fitting with fine-tuned parameters. To mitigate this issue, a convolutional neural network (CNN) was employed to obtain the initial estimates for the c_4, c_{11}

and c_{22} values.

$$RMSE_{wf} = [\sum_j (c_j Z_j)^2]^{1/2} \tag{5}$$

DenseNet121, InceptionV3, and Resnet-50 architectures were trained to estimate the coefficient values. Detailed architectural schemes are provided in additional materials. An input of the networks was a 224x224x3 intensity distribution of the SLB represented as an RGB image. An output linear dense layer provided values for the matrix of the three symmetrical coefficients of the Zernike polynomials. Models were trained using a dataset of 100,000 simulated transversal intensity distributions of the SLB, which were generated using Eq. (3) traced up to 1.5 m.

The ranges of c_j of values used in Eq. (1) and (2) for the generation of the training data were obtained from multiple measurements of SLB wavefronts in the interval L_{PLMIN} and L_{PLMAX} using a well-aligned generator and the SHS. These measurements are presented in the following chapter. The wavefront root-mean-squared error ($RMSE_{wf}$) was calculated using Eq. (5) up to j = 66, excluding piston (c_1), tilts (c_2, c_3), and defocus (c_4) and spherical aberrations (c_{11}, c_{22}), to be in an interval of 0.06 to 0.08λ. The wavefront, therefore, can be approximated by Eq. (1) without significantly affecting the calculation of the zero-phase gradient ring. This is true for most of the generators, such as the ones presented in [30]. One has to be careful when short focal length distance lenses are used as a SLB generator. As a generator consisting of two 5 mm high index ball lenses, the system can be more prone to misalignment and cause a larger influence of non-symmetrical aberrations on the intensity pattern.

Equation (2) was used as noise together with a Gaussian intensity noise with mean zero and variance equal to 1e-7. The amplitude $S_0 = 1$ was assumed. The c_j value intervals in units of [λ] used for training can be seen in Table 1. Note that though the magnitude of the c_{22} is small, it has an important effect on the beam properties due to its symmetry and, therefore, must be used for the description of the SLB wavefront.

Table 1. Interval of c_j values used for training dataset simulations.

Coefficient c_j	[λ]
j = 1	0
j = 4	[-7.85; -1.25]
j = 11	[-2.55; -2.45]
j = 22	[-0.07; -0.08]
$j \in [2, 66] \setminus \{4, 11, 22\}$	[-0.02; 0.02]

The dataset was divided into 80,000 images for testing and 20,000 images for validation. The input images were normalized min-to-max in the interval of [0, 1] to mitigate the influence of intensity, and a square root stretching operation was applied to enhance the shape features. An Adam optimizer using a learning rate 1e-3 was used and halved every 15 epochs down to a minimum value of 5e-6. The batch size was set to 32 using 300 epochs for training. The mean-squared error (MSE) of the c_4, c_{11} and c_{22} values served as the learning metric. The change of a loss function MSE during the training process can be seen in Fig. 3.

InceptionV3 consistently achieved stable validation loss function MSE values, converging to the order of 1e-5. ResNet50 and DenseNet121 exhibited stable validation loss function MSE values in the lower order of 1e-4. To assess the performance of the trained networks, we conducted a reconstruction experiment involving 1,000 wavefronts using simulated data that were not part of the training set. We compared the predicted wavefronts with a reference wavefront by calculating the difference in $RMSE_{wf}$ values. This involved subtracting two sets of coefficient values representing the predicted and reference wavefronts for j in the interval of 4 to 66. This means that the values of $RMSE_{wf}$ were largely influenced by the aberrations introduced by Eq. (2),
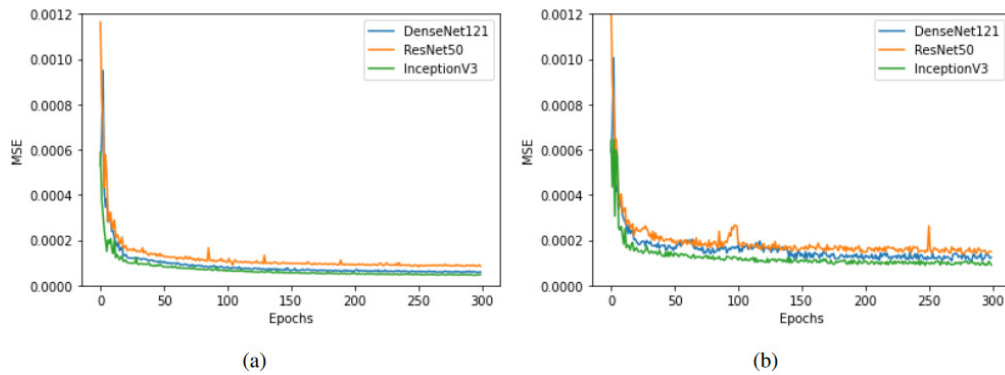
Fig. 3. Loss function changing process of different networks. (a) Training process (b) Validation process. For detailed architectures of ResNet50, InceptionV3, and DenseNet121 see Visualization 1, Visualization 2, and Visualization 3, respectively.

which were not estimated by the AI. The mean values and error bars indicating the standard deviation are presented in Fig. 4. Notably, InceptionV3 outperformed the other architectures, achieving an RMSE of 0.054λ. In contrast, the RMSE values for ResNet50 and DenseNet121 architectures are 0.104λ and 0.096λ, respectively. Consequently, we have selected InceptionV3 for subsequent reconstructions.
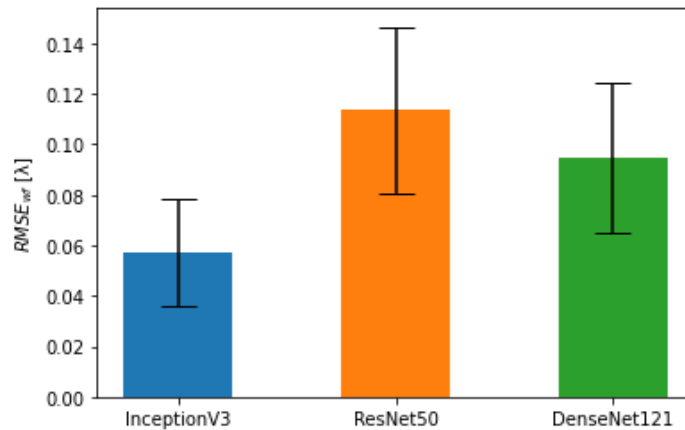

Fig. 4. Mean $RMSE_{wf}$ values of the difference between the reference and predicted wavefront. Error bars represent the standard deviation.

3. Results

3.1. Simulation

The method was validated by reconstructing the wavefront of a simulated intensity distribution with known values of the c_4, c_{11} and c_{22} that were not utilized during the training. Data were generated using the same procedure as for the training data.

The simulated reference intensity distribution, AI estimation followed by the fitting process can be seen in Fig. 5(a), Fig. 5(b) and Fig. 5(c) respectively. The wavefront residual, which represents the difference between the reference wavefront and the wavefront obtained after the fitting, is depicted in Fig. 5(d). For comparative analysis of the c_4, c_{11} and c_{22} the coefficient values can be

seen in Fig. 5(e). The layout presented in this figure is replicated in subsequent figures, each showcasing additional wavefront reconstructions. The $RMSE_{wf}$ values were calculated for the coefficients in the interval from 4 to 66, excluding piston and tilts.
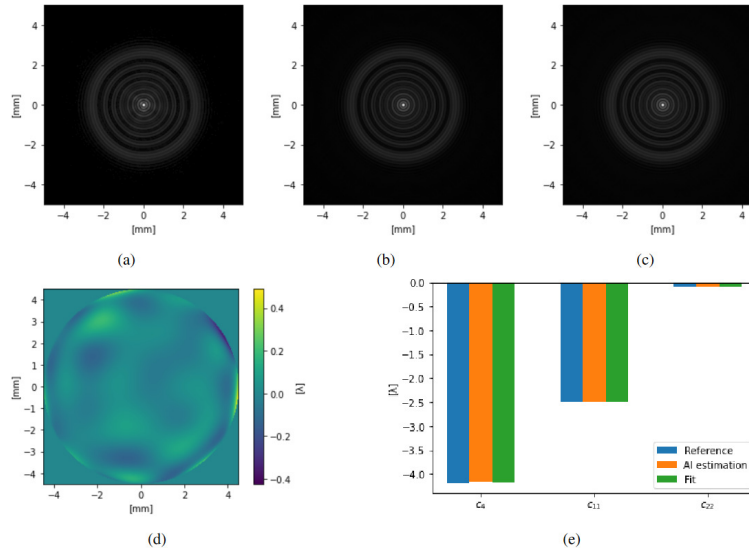

Fig. 5. Validation of the method using simulated data. The square root stretching was used to enhance the features in the intensity distributions. (a) Reference simulated intensity distribution (b) Intensity distribution estimated by artificial intelligence (AI) (c) Intensity distribution obtained through fitting (d) Wavefront residual representing the difference between the reference and fitted wavefront (e) c_j values of reference, AI estimation and fitting for defocus, spherical and secondary spherical aberration

In the measurement displayed in Fig. 5, the percent error for the reference symmetrical coefficients c_4, c_{11} and c_{22} is equal to 0.64% going down to 0.14% after fitting. The $RMSE_{wf}$ between the reference and the fitting process stands at 0.057λ after including the error of the non-symmetrical coefficients up to c_{66}. The peak-to-valley (PV) wavefront difference between the initially generated reference and the wavefront obtained through fitting measures at 0.89λ.

The percent errors in the measurement presented in Fig. 6 are equal to 0.38% and 0.37% for prediction and fitting respectively. The $RMSE_{wf}$ is equal to 0.077λ after fitting. The peak-to-valley (PV) wavefront difference is measured to be 0.74λ.

The method has been effectively applied to data that were not part of the training dataset. Fitting reduces the error of the AI estimation even when only the c_4, c_{11} and c_{22} are the subject of change. As a result, the coefficients used to generate the SLB are estimated with slightly higher accuracy. Using AI estimation alone is up for consideration, reducing the method's runtime from seconds to milliseconds without significantly sacrificing accuracy. The main major portion of the $RMSE_{wf}$ are the aberrations induced by Eq. (2).

3.2. Experiments

Wavefronts of several SLBs were measured using the SHS sensor and taken as a reference. The intensity distributions were measured using the camera placed 1.5 m away from the generator. The images were taken with low exposure values in order. Hence, pixels are not saturated. The image was cut to have a size 10x10 mm, and the resolution was lowered to match the input size of the InceptionV3 network. Two laser source with a wavelength of 532 nm and power of 0.9 mW
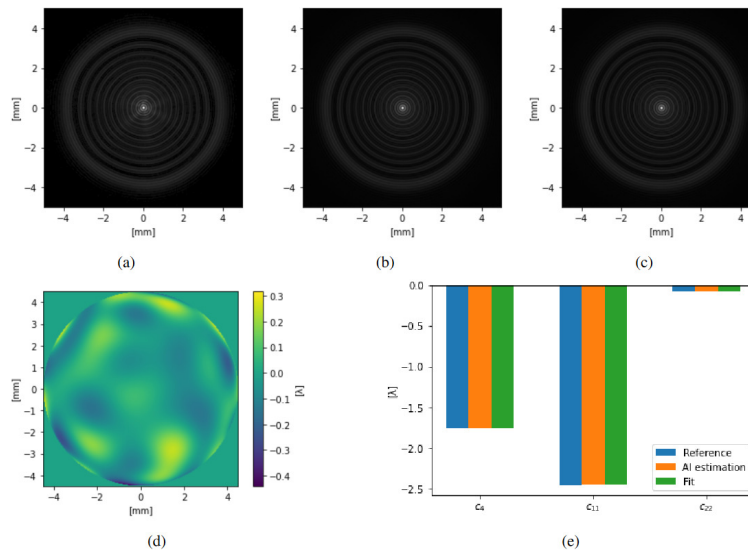
Fig. 6. Validation of the method using simulated data. The square root stretching was used to enhance the features in the intensity distributions. (a) Reference simulated intensity distribution (b) Intensity distribution estimated by artificial intelligence (AI) (c) Intensity distribution obtained through fitting (d) Wavefront residual representing the difference between the reference and fitted wavefront (e) c_j values of reference, AI estimation and fitting for defocus, spherical and secondary spherical aberration

was used for measurements in Figs. 7 and 8. For measurements in Figs. 9 and 10, a laser source with a power of 4.5 mW with a wavelength of 532 nm was used.

In the wavefront estimation depicted in Fig. 7 the percent error for the reference symmetrical coefficients c_4, c_{11} and c_{22} is equal to 0.57% going down to 0.45% after fitting. The $RMSE_{wf}$ equals to 0.088λ after fitting. Simultaneously, the peak-to-valley (PV) wavefront difference between the initially generated reference and the wavefront obtained through fitting measures at 1.15λ.

In the measurement presented in Fig. 8, the $RMSE_{wf}$ stands at 0.081λ after fitting. The percent error of the defocus and spherical aberrations is equal to 0.24% and 0.15% for AI prediction and fitting, respectively. The PV wavefront difference between the generated reference and the wavefront was obtained through fitting measures at 0.88λ.

Experiments effectively demonstrate the method's utility in estimating the wavefront of an SLB, specifically the coefficients c_4, c_{11}, and c_{22}. Notably, despite the AI model being trained on a simulated dataset, it proves to be highly effective when applied to real measurements.

In the measurement presented in Fig. 9, the $RMSE_{wf}$ is equal to 0.085λ after fitting. The percent errors of the c_4, c_{11} and c_{22} for the AI estimation is equal to 1.47% and 0.52% for the fitting. The peak-to-valley (PV) wavefront difference between the initially generated reference and the wavefront obtained through fitting measures at 1.12λ.

In the wavefront estimation shown in Fig. 10, the percent error of the AI estimation is equal to 1.45% decreasing down to 0.12% after using the fitting. The $RMSE_{wf}$ stands at 0.082λ after using the fitting process. Simultaneously, the peak-to-valley (PV) wavefront difference between the initially generated reference and the wavefront obtained through fitting measures at 0.92λ.

An increase in the reconstruction error for the coefficients c_4, c_{11}, and c_{22} of the AI estimation is apparent for both measurements in Figs. 9 and 10. This increase could be attributed to the utilization of a different laser source with higher power and a distinct spatial illumination
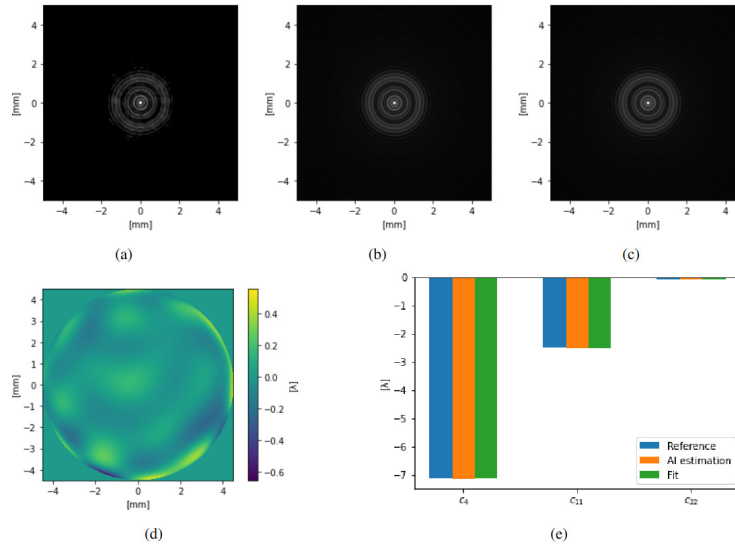
Fig. 7. Validation of the method using a comparison with a SHS wavefront measurement. The square root stretching was used to enhance the features in the intensity distributions. (a) Measured intensity distribution (b) Intensity distribution estimated by artificial intelligence (AI) (c) Intensity distribution obtained through fitting (d) Wavefront residual representing the difference between the reference and fitted wavefront (e) c_j values of measured reference, AI estimation and fitting for defocus, spherical and secondary spherical aberration
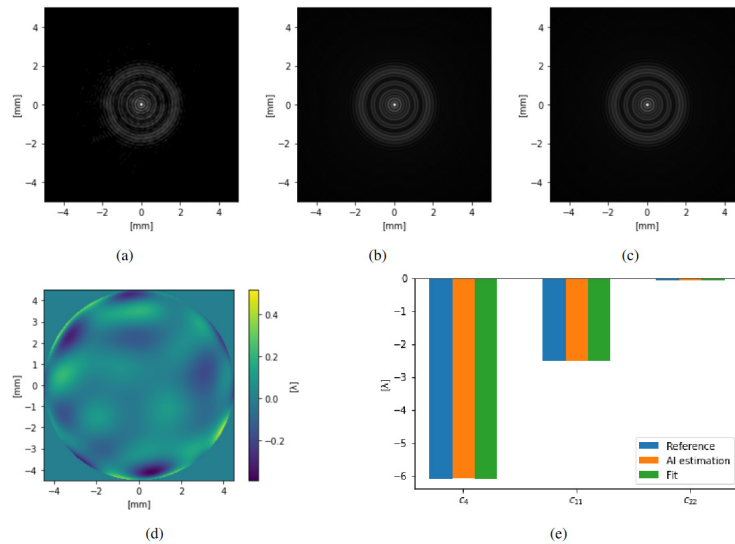

Fig. 8. Validation of the method using a comparison with a SHS wavefront measurement. The square root stretching was used to enhance the features in the intensity distributions. (a) Measured intensity distribution (b) Intensity distribution estimated by artificial intelligence (AI) (c) Intensity distribution obtained through fitting (d) Wavefront residual representing the difference between the reference and fitted wavefront (e) c_j values of measured reference, AI estimation and fitting for defocus, spherical and secondary spherical aberration
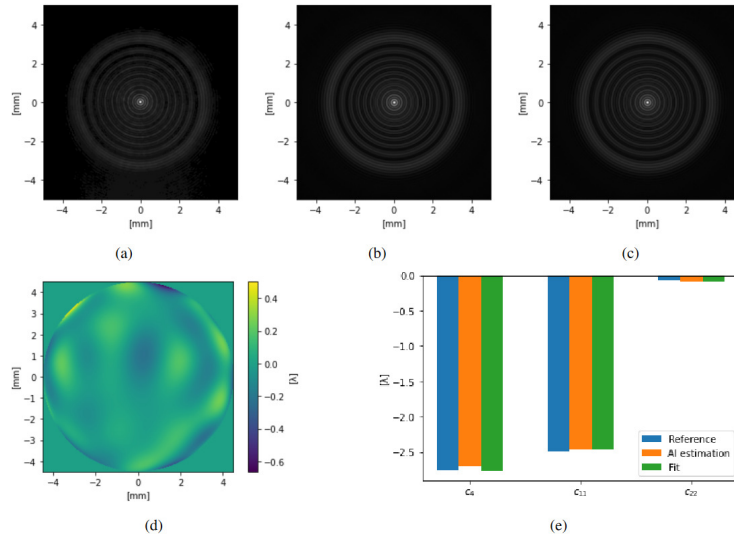
Fig. 9. Validation of the method using a comparison with a SHS wavefront measurement. The square root stretching was used to enhance the features in the intensity distributions. (a) Measured intensity distribution (b) Intensity distribution estimated by artificial intelligence (AI) (c) Intensity distribution obtained through fitting (d) Wavefront residual representing the difference between the reference and fitted wavefront (e) c_j values of measured reference, AI estimation and fitting for defocus, spherical and secondary spherical aberration
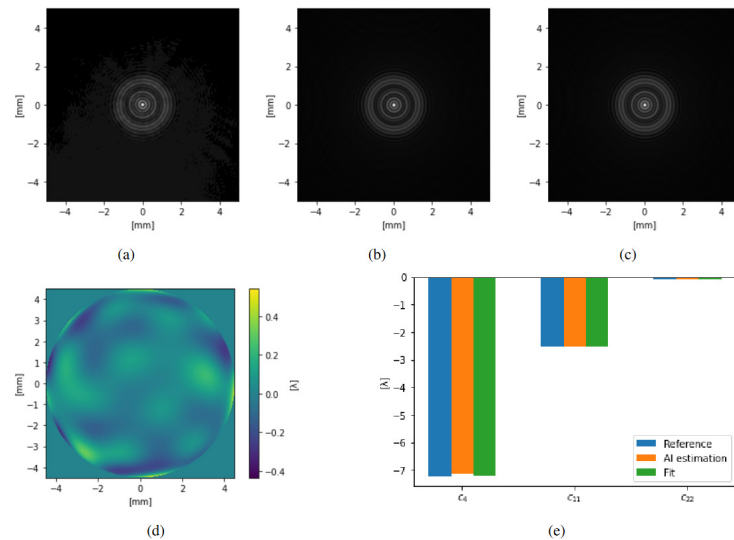

Fig. 10. Validation of the method using a comparison with a SHS wavefront measurement. The square root stretching was used to enhance the features in the intensity distributions. (a) Measured intensity distribution (b) Intensity distribution estimated by artificial intelligence (AI) (c) Intensity distribution obtained through fitting (d) Wavefront residual representing the difference between the reference and fitted wavefront (e) c_j values of measured reference, AI estimation and fitting for defocus, spherical and secondary spherical aberration

distribution than for the previous measurements. After closely examining the figures, a stray light outside of the SLB's outer ring can be seen. This can cause an increase in the AI estimation error.

If we compare the reconstructed and measured reference wavefronts from the experiments, the zero-phase gradient ring can be calculated with an error of less than 10 μm for all of the presented reconstructions.

4. Discussion

The results obtained from this study show the advantage of using AI combined with least-squares fitting to estimate the SLB wavefront, and its characteristics, using symmetrical defocus (c_4) and spherical aberrations (c_{11}, c_{22}) with a root-mean-squared error of the wavefront estimation being smaller than 0.09λ. This approximation by symmetrical aberrations is enabled by the fact that non-symmetrical aberrations in the SLB wavefront have low magnitudes, considering the SLB generators used in long-distance alignment. Note that using lenses with shorter focal lengths can cause the generator to be susceptible to misalignment and to the effect of non-symmetrical aberrations.

While the AI estimation of the Zernike polynomial coefficients alone demonstrates satisfactory results, the switch to a different laser source decreased the accuracy of the AI estimation. The AI performance could be improved by increasing the number of samples used for training or possibly by incorporating an illumination distribution change into the training dataset generation process. Training on real data could improve the results. However, this process can be labor-intensive for large datasets. The subsequent least-squares fitting process generally refines the estimation of these coefficients, leading to higher precision. The trade-off between the accuracy gain and time span of the method needs to be considered when it comes to the use of the fitting, which can be rendered unnecessary. Importantly, despite being trained on simulated data, the CNN was successfully applied to measured data from the laboratory, with results aligning with the SHS measurements.

By accurately estimating the wavefront, describing it using the dominant defocus and spherical aberrations produced by the SLB generator, it becomes feasible to determine the beam properties. Notably, the zero-phase gradient ring, which affects the size of the SLB core. This assessment will be beneficial for ensuring beam quality in precision-demanding applications such as long-distance accelerator alignment. The simulation approach employed in this study allows to generate non-diffracting beams through aberrations and can offer a straightforward means to obtain a desired beam shape through the manipulation of the induced aberrations.

References

1. H. Durand Mainaud, S. B. Jimenez, T. Dijoud, M. Duquenne, A. Herty, and K. Kucel, "HL-LHC alignment requirements and associated solutions," in *Proceedings 8th Int. Particle Accelerator Conference (IPAC'17)*, (2017), pp. 1893–1896.
2. CERN, "The Compact Linear Collider (CLIC)," https://home.cern/science/accelerators/compact-linear-collider.
3. FCC collaboration, others, "FCC-ee: the lepton collider: future circular collider conceptual design report volume 2," Eur. Phys. J. Spec. Top. **228**(2), 261–623 (2019).
4. G. Stern, "Study and development of a laser based alignment system for the compact linear collider," Ph.D. thesis, ETH Zurich (2016).

5. T. Suwada, M. Satoh, S. Telada, and K. Minoshima, "Propagation and stability characteristics of a 500-m-long laser-based fiducial line for high-precision alignment of long-distance linear accelerators," Rev. Sci. Instrum. **84**(9), 093302 (2013).

6. L. V. Griffith, R. F. Schenz, and G. E. Sommargren, "Magnetic alignment and the poisson alignment reference system," Rev. Sci. Instrum. **61**(8), 2138–2154 (1990).

7. D. Kaemtner and J. Prenting, "Straight Line Reference System (SLRS) for the Adjustment of the X-ray Free-electron Laser (XFEL) at DESY," in *Proceedings of the 9th International Workshop on Accelerator Alignment (IWAA)*, Stanford Linear Accelerator Center (SLAC), California, United States, (2006).

8. M. Beker, G. Bobbink, B. Bouwens, *et al.*, "The rasnik 3-point optical alignment system," J. Instrum. **14**(08), P08010 (2019).

9. C. Zhang, M. Hasegawa, K. Kanda, and T. Shinomoto, "Performance of the iris diaphragm laser alignment system of the SPring-8," in *Proceedings of 13th Int. Workshop on Accelerator Alignment (Beijing, China)*, (2014).

10. J. Gayde and M. Sulc, "An optical system for producing a structured beam," EP3564734 (2019).

11. J. Durnin, "Exact solutions for nondiffracting beams," J. Opt. Soc. Am. A **4**(4), 651–654 (1987).

12. J. Durnin, J. Miceli, and J. H. Eberly, "Comparison of bessel and gaussian beams," Opt. Lett. **13**(2), 79–80 (1988).

13. Y. Shen, S. Pidishety, I. Nape, and A. Dudley, "Self-healing of structured light: a review," J. Opt. **24**(10), 103001 (2022).

14. R. Parks, "Alignment using axicon plane gratings," Proc. SPIE **10747**, 1074703 (2018).

15. R. E. Parks, "Aligning reflecting optics with bessel beams," Proc. SPIE **11488**, 114880J (2020).

16. R. E. Parks, "Practical considerations for using grating produced bessel beams for alignment purposes," Proc. SPIE **11816**, 1181603 (2021).

17. R. E. Parks, "Rapid centering of optics," Proc. SPIE **11889**, 118890V (2021).

18. D. M. Gale, "Visual alignment of mechanical structures using a bessel beam datum: practical implementation," Proc. SPIE **8082**, 80823D (2011).

19. S. N. Khonina, V. V. Kotlyar, V. A. Soifer, *et al.*, "Astigmatic bessel laser beams," J. Modern Opt. **51**(5), 677–686 (2004).

20. H. Cheng, C. Xia, S. M. Kuebler, *et al.*, "Aberration correction for slm-generated bessel beams propagating through tilted interfaces," Opt. Commun. **475**, 126213 (2020).

21. R. Dwivedi, P. Sharma, V. Kumar, *et al.*, "Axicon aberration leading to short-range nondiverging optical array and elliptical dark hollow beam," Opt. Eng. **57**(5), 055106 (2018).

22. J. Dudutis, R. Stonys, G. Račiukaitis, *et al.*, "Glass dicing with elliptical bessel beam," Opt. Laser Technol. **111**, 331–337 (2019).

23. S. N. Khonina, V. D. Paranin, A. V. Ustinov, *et al.*, "Astigmatic transformation of bessel beams in a uniaxial crystal," Opt. Appl. **46**, 5–18 (2016).

24. S. N. Khonina, S. V. Karpeev, and V. D. Paranin, "Birefringence detection of a gradient-index lens based on astigmatic transformation of a bessel beam," Optik **164**, 679–685 (2018).

25. S. N. Khonina, N. L. Kazanskiy, P. A. Khorin, *et al.*, "Modern types of axicons: New functions and applications," Sensors **21**(19), 6690 (2021).

26. B. Miao, L. Feder, J. E. Shrock, *et al.*, "Phase front retrieval and correction of bessel beams," Opt. Express **30**(7), 11360–11371 (2022).

27. G. Allan, I. Kang, E. S. Douglas, G. Barbastathis, and K. Cahoy, "Deep residual learning for low-order wavefront sensing in high-contrast imaging systems," Opt. Express **28**(18), 26267–26283 (2020).

28. S. W. Paine and J. R. Fienup, "Machine learning for improved image-based wavefront sensing," Opt. Lett. **43**(6), 1235–1238 (2018).

29. Y. Nishizaki, M. Valdivia, R. Horisaki, *et al.*, "Deep learning wavefront sensing," Opt. Express **27**(1), 240–251 (2019).

30. W. Niewiem, K. Polak, M. Dusek, D. Mergelkuhl, J.-C. Gayde, A. Wieser, and M. Sulc, "Variation of structured laser beam pattern and optimization for an alignment reference line creation," Optics Express (to be published) (2023).

31. J.-C. Gayde, M. Sulc, and K. Polak, "Introduction to structured laser beam for alignment and status of the R&D," (2022).

32. R. M. Herman and T. A. Wiggins, "Production and uses of diffractionless beams," J. Opt. Soc. Am. A **8**(6), 932–942 (1991).

33. Z. von F, "Beugungstheorie des schneidenver-fahrens und seiner verbesserten form, der phasenkontrastmethode," Physica **1**(7-12), 689–704 (1934).

34. R. J. Noll, "Zernike polynomials and atmospheric turbulence," J. Opt. Soc. Am. **66**(3), 207–211 (1976).

35. M. Dusek, "Advanced calibration and characterization of a Shack-Hartmann sensor," Master's thesis, Technical University of Liberec (2021).